

# Radial displacement of pellet ablation material in tokamaks due to the grad-B effect\*

P. B. Parks,<sup>†,a)</sup> W. D. Sessions,<sup>b)</sup> and L. R. Baylor<sup>c)</sup>  
*General Atomics, P.O. Box 85608, San Diego, California 92186-5608*

(Received 15 November 1999; accepted 11 February 2000)

During pellet injection in tokamaks, a rapid movement of pellet ablation substance towards the low-field or outward major radius  $R$  direction is observed, favoring pellet injection from the high-field side in order to promote deeper fuel penetration. The motion has been attributed to a vertical curvature and  $\nabla B$  drift current induced inside the ionized ablated material by the  $1/R$  toroidal field variation. The uncompensated vertical drift current inside the weakly diamagnetic ( $\beta < 0.1$ ) ablation cloud will cause charge separation at the boundary. The resulting electrostatic field induces the  $E \times B$  drift to the large- $R$  side of the torus. The calculated fuel penetration depth is consistent with inside launched pellet experiments on the DIII-D tokamak [J. L. Luxon and L. G. Davis, *Fusion Technol.* **8**, 441 (1985)]. The dependence of the penetration depth with plasma parameters suggests that low velocity inside launched pellets may provide a unique solution to the refueling problem in larger and hotter machines of the future. © 2000 American Institute of Physics. [S1070-664X(00)97005-8]

## I. INTRODUCTION

Fueling the central region of a tokamak plasma by hydrogen pellet injection seems to provide favorable conditions for accessing enhanced confinement regimes in present day tokamaks. Core fueling in future burning plasmas could be advantageous because it would maximize tritium burnup and achieve greater fusion power by peaking the density profile. Normally, pellets are injected from the outside wall or low magnetic field side (LFS) of a tokamak, where exceedingly high velocities  $>10$  km/s will be needed to achieve deep penetration in a large fusion plasma.

Recently, Lang *et al.* drew attention to the possibility of enhancing fuel penetration by injecting  $D_2$  pellets from the inside wall or high-field side (HFS) of the Axisymmetric Divertor Experiment, Upgrade.<sup>1</sup> The ablated and ionized pellet substance apparently drifts in the direction of the major radius  $R$ , and thus HFS pellet injection favors deeper fuel penetration compared with standard LFS pellet injection. Since then, experiments in the DIII-D tokamak verify that inside launched pellets injected at an angle of  $45^\circ$  above the equatorial plane deposit fuel closer to the plasma core and well beyond the pellet range of throw.<sup>2</sup>

This movement of pellet ablation material in the large- $R$  direction can be attributed to the  $1/R$  variation of the toroidal magnetic field  $B$ . Magnetic-curvature and  $\nabla B$ -induced charged particle drifts produce a charge separation layer inside the ionized part of the pellet ablation cloud, as shown in Fig. 1. This part of the cloud is a weakly diamagnetic plasmod, with a magnetic beta,  $\beta = p/(B^2/2) < 0.1$ , where  $p$  is

the pressure. This  $\beta$  value is almost always higher than the surrounding plasma beta  $\beta_\infty$ . The excess  $\beta$  leads to an uncompensated curvature and  $\nabla B$  drift current given by

$$J_{\nabla B} = \frac{-2p}{RB}. \quad (1)$$

Under open circuit conditions, this current is cancelled by an opposing ion polarization current

$$J_p = \frac{\rho}{B^2} \frac{dE}{dt}, \quad (2)$$

where  $\rho$  is the mass density, and  $E$  is the charge induced electric field. Hence the  $E \times B$  drift velocity of the cloud is given by

$$\frac{dv_\perp}{dt} = \frac{2p}{\rho R}, \quad (3)$$

where the acceleration points in the direction of the major radius. Initially, the cloud accelerates at  $\sim 10^8 \text{ ms}^{-2}$  and reaches a velocity far exceeding the pellet velocity on a very fast time scale  $\sim 100 \mu\text{s}$ . Since the  $\beta$  of the ionized part of the ablation cloud is initially very low, it moves across the  $B$  field without significantly distorting the  $B$  field.

This simple physical picture is incomplete because, first of all, expansion of the cloud along the magnetic field lines at its own sound speed causes pressure relaxation, and the relaxation rate requires the specification of initial cloud conditions. In Sec. II we begin by characterizing the dimensions and plasma parameters of the ionized ablation channel using a simple one-dimensional (1D) steady-state flow model. A pellet cloud instability, considered responsible for the observed pellet cloud striations, periodically separates this part of the cloud from the pellet forming a  $\beta < 0.1$  detached cloudlet. We make the *ad hoc* assumption that the initial conditions of the cloudlet are inherited from the ionized ablation channel at the moment of separation.

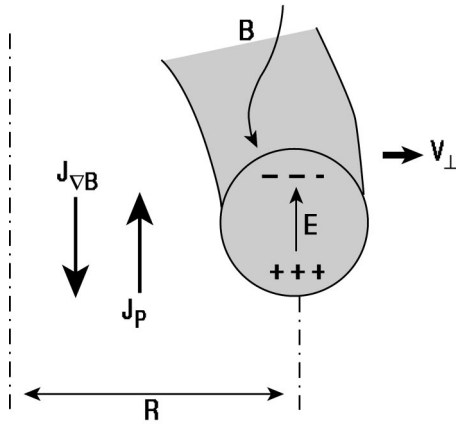
\*Paper UI 15 Bull. Am. Phys. Soc. **44**, 288 (1999).

<sup>†</sup>Invited speaker.

<sup>a)</sup>Electronic mail: parks@gat.com

<sup>b)</sup>Also with: Tennessee Technological University, Cookeville, Tennessee.

<sup>c)</sup>Also with: Oak Ridge National Laboratory, Oak Ridge, Tennessee.

FIG. 1. Physical mechanisms of large- $R$  pellet cloud drift.

Section III describes the subsequent expansion of the cloudlet along the magnetic field lines using a Lagrangian fluid simulation code. The cross-field acceleration ceases when equilibrium with the background plasma pressure is attained, i.e.,  $\nabla_{\parallel} p = 0$  along the field lines. In Sec. IV, we solve for the electrostatic potential inside and outside the moving cloudlet and find its  $E \times B$  drift velocity. We consider charge layer depletion by parallel current flows associated with the emission of Alfvén waves.<sup>3–6</sup> This leads to a drag on the cloud, causing it to stop shortly after arriving at pressure equilibrium. Assuming uniform plasma profiles, we can obtain scaling laws for the stopping, or penetration distance in the outward major radius direction (Sec. V). The calculated fuel penetration distance  $\sim 30$  cm appears to be consistent with HFS pellet injection experiments in DIII-D.<sup>2</sup> The scaling laws illustrate that deeper penetration will result for larger pellets and higher temperature and density plasmas. We conclude our discussion in Sec. VI.

## II. INITIAL CONDITIONS

### A. Low- $\beta$ ionized ablation channel

In the immediate vicinity of the pellet the surrounding ablation cloud is a cold, dense neutral gas. The ablation flow starts out moving at subsonic velocities and then accelerates to mildly supersonic velocities by the heating resulting from the absorption of the parallel heat flux carried by incident plasma electrons. The transition from subsonic to supersonic motion occurs at the sonic radius  $r^* \cong 1.6r_p$ , where  $r_p$  is the radius of the pellet. It is useful to characterize the magnitude of the ablation  $\beta$  and temperature  $T$  in this inner flow domain by their respective values at the sonic radius<sup>7–9</sup>

$$\beta_{*'} = 4.3 \times 10^3 \left( \frac{W}{n_{e\infty} r_p \ln \Lambda_{\text{en}}} \right)^{1/3} T_{e\infty}^{2/3} \beta_{\infty}, \quad (4)$$

$$T_{*'} = 1.88 \times 10^{-9} \left( \frac{W}{T_{e\infty}} \right)^{1/3} (n_{e\infty} r_p \ln \Lambda_{\text{en}})^{2/3},$$

where  $W$  is the pellet atom mass in amu,  $T_{e\infty}$  and  $n_{e\infty}$  are, respectively, the electron temperature and density of the surrounding plasma,  $\Lambda_{\text{en}} = 2T_{e\infty}/7.5$ , and eV cm units are used. For example, the experimental parameters for inside

launched D<sub>2</sub> pellets in DIII-D are:  $B = 3$  T,  $T_{e\infty} = 1.3$  keV,  $n_{e\infty} = 7 \times 10^{13} \text{ cm}^{-3}$  and  $r_p = 0.05$  cm, which gives  $\beta_{\infty} = 0.008$ ,  $\beta_{*'} = 0.19$ , and  $T_{*'} = 0.16$  eV. For partial penetration of deuterium–tritium pellets in fusion grade plasmas:  $B = 5$  T,  $T_{e\infty} = 5$  keV,  $n_{e\infty} = 10^{14} \text{ cm}^{-3}$  and  $r_p = 0.3$  cm, we find  $\beta_{\infty} = 0.016$ ,  $\beta_{*'} = 0.46$ , and  $T_{*'} = 0.54$  eV. Although these cloud  $\beta$ s are nearly of order unity, one finds that even under fusion plasma conditions the inner flow domain near the pellet is unaffected by the magnetic field because the gas is unionized and nonconducting at these temperatures and pressures.

The cloud pressure and  $\beta$  decay rapidly with distance from the pellet due to radial expansion. Simultaneously, the cloud becomes more ionized and conducting with distance until at some point the magnetic field force brakes the transverse motion and funnels the flow into a low- $\beta$  ionized “ablation channel.”

### B. Cloudlet formation—striations

The dynamics of the outer flow domain are complicated by the occurrence of irregular structures and periodicity. Time-integrated photographs show a striated ablation trail, consisting of a pattern of alternating rows of light–dark zones aligned with the  $B$  field.<sup>10</sup> This pattern correlates with oscillations in the  $D_{\alpha}$  line emission intensity. There appears to be no unambiguous correlation of the minima in the  $D_{\alpha}$  signal with the pellet crossing a sequence of rational  $q$  surfaces<sup>11,12</sup> ( $q$  = safety factor), which might drain part of the plasma energy content of a closed flux tube. Recently, more detailed experimental evidence indicates that the striations are the result of the ionized ablation channel being periodically *separated* from the pellet.<sup>12,13</sup> The underlying mechanism is thought to be an  $E \times B$  rotationally driven magnetic interchange instability,<sup>14</sup> because these modes explain many features of the observed striations.<sup>12</sup> The linear theory finds that the fastest growing mode, the  $m = 1$  shift mode, grows exponentially on the time scale  $\gamma_{E \times B}^{-1} = (0.025 T_{e\infty}/eBr_{\perp}^2)^{-1}$ , where  $r_{\perp} \sim 10r_p$  is the channel radius. Usually,  $\gamma_{E \times B}^{-1}$  is comparable to the time scale for buildup of the ablation channel  $\sim 10$ – $30 \mu\text{s}$ . The absence of magnetic shear on the local scale of the ablation channel means that these modes can completely interchange flux tubes, converting a shielding channel into a “detached cloudlet” (Fig. 2). Subsequently, the cloudlet expands along the field lines while drifting as a whole across the magnetic field. Rapid expansion causes the density to drop and heating increases the ionization level. Both effects reduce the light emission so that cloudlet formation corresponds to a dark zone. A new ablation channel is formed on about the same time scale forming a bright zone and the process repeats.

These periodic “cloud disruptions” breed a sequence of  $N = \tau_{\text{life}} \gamma_{E \times B}^{-1} \sim 20$  or more discrete cloudlets along the trajectory of the pellet, where  $\tau_{\text{life}}$  is the pellet lifetime. Each cloudlet carries off the ablated mass contained in the ablation channel at the moment of its birth. We propose that the initially detached cloudlet possesses a cylindrical shape with radius and length equal to that of the ablation channel. In

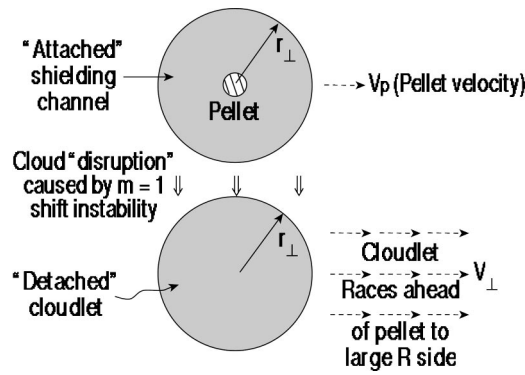


FIG. 2. The  $m=1$  shift mode separates the ablation channel from the pellet forming a discrete “cloudlet.” Subsequently the cloudlet drifts to the right.

addition, we imagine that the parallel flow profiles of the newly formed cloudlet are inherited from the parallel flow profiles of the ablation channel.

### C. Parallel flow model for the attached ablation channel

The ablation channel resembles a “flexible magnetic nozzle” with cross-sectional area  $A(s)$  varying slowly with axial distance  $s$  parallel to the magnetic field. Combining the transverse force balance equation  $p(s) + B^2(s)/2 = p_\infty + B_\infty^2/2 \approx B_\infty^2/2$ , with the magnetic flux conservation equation  $B(s)A(s) = \text{const}$ , one obtains  $A(s)/A_0 = \sqrt{(1 - \beta_0)/[1 - \beta_0 p(s)/p_0]}$ , where the subscript 0 denotes a variable at the channel entrance,  $s=0$ . As mentioned, the entrance  $\beta_0$  is small, we will show that  $\beta_0 < 0.1$ , and hence the contraction of the channel cross section from entrance to exit amounts to less than 5%. We therefore assume constant area circular cross section  $A(s) = \pi r_\perp^2$ , and borrow standard 1D duct flow expressions that relate the flow variables at one location with Mach number  $M = v/c_s$  to their corresponding values at the sonic  $M=1$  location downstream, denoted by the *unprimed* asterisk

$$\begin{aligned} \frac{p}{p_*} &= \frac{1 + \gamma}{1 + \gamma M^2}, \quad \frac{T}{T_*} \equiv \Theta(M) = \frac{(1 + \gamma)^2 M^2}{(1 + \gamma M^2)^2}, \\ \frac{n}{n_*} &\equiv Y(M) = \frac{1 + \gamma M^2}{(\gamma + 1) M^2}, \\ \frac{h_t}{h_{t*}} &\equiv H(M) = \frac{(1 + \gamma) M^2 [2 + (\gamma - 1) M^2]}{(1 + \gamma M^2)^2}, \end{aligned} \quad (5)$$

where total specific stagnation enthalpy is  $h_t = c_s^2/(\gamma - 1) + v^2/2$ ,  $\gamma = 5/3$ , and  $c_s = \sqrt{2\gamma T/m_i}$ , with  $m_i$  being the ion mass. In the pellet frame of reference, the toroidal drift effect causes the shielding channel to bend gradually with distance  $s$  in the direction of the major radius.<sup>15</sup> The axial distance where the centroid of the channel has shifted by an amount equal to its radius denotes the effective shielding length  $s = L_c \sim (r_\perp R)^{1/2}$ . At that point, the ablation flow field is no longer magnetically entrained and “spills” into the background plasma while spreading freely along the magnetic field lines in *both* directions. This point is analogous to the exit point of a jet issuing from a circular pipe into an ambient

medium with lateral spreading downstream. Internal heating supplied by the deposition of the incident plasma electrons drives the Mach number toward unity. When the pressure of the ambient medium is below the exit pressure—the under-expanded jet—the system is choked with  $M=1$  at the pipe exit. The same kind of sonic exit condition applies here because  $\beta_\infty$  is usually lower than the exit beta  $\beta_*$ , which has a lower bound  $\beta_0/(1 + \gamma)$ , according to Eq. (5).

Cloud heating is based on a kinetic treatment for the deposition of energy by plasma electrons incident on the cloud with a half-space Maxwellian distribution of temperature  $T_{e\infty} \gg T$ . In passing through a column density  $\tau = \int n ds$ , the energy flux carried by the incident electrons  $q$  is attenuated by the amount<sup>16</sup>  $\eta \equiv q/q_\infty = 0.5uK_2(u^{1/2})$ , in which  $u = \tau/\tau_\infty$ ,  $\tau_\infty (\text{cm}^{-2}) = 2.24 \times 10^{12} T_{e\infty}^2 (\text{eV}) / \ln \Lambda_{ee}$  is the characteristic range of penetration for hot Maxwellian electrons in cold plasma,  $K_2$  is a standard modified Bessel function, and  $q_\infty = (2/\pi m_e)^{1/2} n_{e\infty} T_{e\infty}^{3/2} \exp(-\Delta\Phi/T_{e\infty})$ , with the sheath potential drop<sup>14</sup> at the channel-plasma interface being  $\Delta\Phi \approx 1.8T_{e\infty}$ . The energy balance equation  $q_* - q = (G/2A)(h_{t*} - h_t)$ , with  $q_* = q_\infty$ , and  $G = \text{pellet mass ablation rate}$ , gives  $\eta(M; M_0, \eta_0) = 1 - (1 - \eta_0)(1 - H)/(1 - H_0)$ . Combining this expression with the channel density in Eq. (5), and using a more convenient three parameter fitting function  $\eta \approx \eta_{\text{fit}} = \exp[-\alpha[(u + \bar{u})^\lambda - \bar{u}^\lambda]]$  we can obtain  $M(x)$  from  $dM/dx = \Sigma_0 F(M; M_0, \eta_0)$ , where  $x = s/L_c$ ,  $\Sigma_0 = n_0 L_c / \tau_\infty$  is the normalized cloud opacity,

$$F = \frac{\alpha \lambda}{4(\gamma + 1)^2 Y_0} \left( \frac{1 - H_0}{1 - \eta_0} \right) \frac{(1 + \gamma M^2)^4 \eta}{M^3 (1 - M^2) (\bar{u}^\lambda - \alpha^{-1} \ln \eta)^{1/\lambda - 1}} \quad (6)$$

and  $\alpha = 0.3$ ,  $\lambda = 0.7$ ,  $\bar{u} = 0.56$ . Given the two channel entrance properties,  $M_0$  and  $n_0$  (or  $\Sigma_0$ ), a consistency condition

$$\Sigma_0 = \int_{M_0}^1 F^{-1} dM \quad (7)$$

uniquely determines the total channel attenuation coefficient  $\eta_0$ . The channel entrance temperature  $T_0 \sim 2$  eV as required by nearly complete ionization. Hence, the Mach number and all the other flow profiles in the shielding channel are now known. From mass conservation:  $G = 2\pi r_\perp^2 m_i n_0 M_0 c_{s0}$ , and the known scaling laws for  $G$ , we can infer  $n_0$ , and hence  $\Sigma_0$ , and  $\beta_0/\beta_\infty$ :

$$n_0 = \frac{1.3 \times 10^{15} n_{e\infty}^{1/3} T_{e\infty}^{11/6}}{M_0 \kappa_c^2 W^{1/3} c_{s0} r_p^{2/3} (\ln \Lambda_{en})^{2/3}}, \quad (8)$$

$$\Sigma_0 = \frac{582 R^{1/2}}{M_0 \kappa_c^{3/2} W^{1/3} c_{s0}} \left( \frac{n_{e\infty}^2}{T_{e\infty} r_p} \right)^{1/6} \frac{\ln \Lambda_{ee}}{(\ln \Lambda_{en})^{2/3}}, \quad (9)$$

$$\frac{\beta_0}{\beta_\infty} = \frac{406 c_{s0} T_{e\infty}^{5/6}}{M_0 \kappa_c^2} \left( \frac{W}{n_{e\infty} r_p \ln \Lambda_{en}} \right)^{2/3}, \quad (10)$$

where  $\kappa_c \equiv r_\perp / r_p$ . The scaling of this parameter is not yet resolved since it depends on the details of the 2D ablation flow in the transition region between the channel entrance and the  $M > 1$  spherically symmetric flow domain near the

pellet. One approach is to consider the conservation of energy flow across a control surface enclosing the entire ablation cloud, namely

$$2\pi r_{\perp}^2 q_{\infty}(1 - \mu_E) = G(4\gamma T_* + \varepsilon_{\text{ion}} + \varepsilon_{\text{diss}})/m_i, \quad (11)$$

which then yields

$$\kappa_c = \frac{1.54 \times 10^4 T_{e\infty}^{1/6}}{(1 - \mu_E)^{1/2} W^{1/6} (n_{e\infty} r_p \ln \Lambda_{\text{en}})^{1/3}} (4\gamma T_* + \varepsilon_{\text{ion}} + \varepsilon_{\text{diss}})^{1/2}, \quad (12)$$

where  $\varepsilon_{\text{ion}} = 13.6 \text{ eV/ion}$  is the latent energy of ionization,  $\varepsilon_{\text{diss}} = 2.2 \text{ eV/ion}$  is the dissociation energy, and  $\mu_E$  is the heat-flux attenuation coefficient for the Maxwellian electron passing through the entire length of the ablation cloud ( $\mu_E = 1$  means no attenuation). In Ref. 14, Eq. (18) defines its counterpart  $\mu$  as the particle flux attenuation coefficient, and it is a function of radius from the axis of the cloud where pellet occlusion makes  $\mu = 0$ . Here,  $\mu_E$  represents an appropriately averaged value over the cloud cross section. The strength of the magnetic field, which would seem to matter, is concealed in this scaling law. The reason is that the retarding magnetic force is proportional to  $B^2 \times (\text{electrical conductivity})$ , which varies strongly with temperature at the onset of ionization. Hence, the cloud exit temperature  $T_*$  appearing in Eq. (12) has only a weak dependence on the magnitude of the  $B$  field because it is essentially pinned at  $T_0 \sim 2 \text{ eV}$  (see Fig. 3). If we take  $\mu_E = 0.5$  then the scaling law seems to be consistent with cloud width measurements during  $\text{D}_2$  pellet injection experiments,<sup>10</sup> and a limited number of 2D numerical simulations.<sup>9</sup>

The value of  $M_0$  appearing in Eqs. (8) and (9) is also not yet clear; however, we note that a shock front must exist in the transition region, where the upper bound on the preshock Mach number is  $^{7} (5/\gamma)^{1/2} = 3^{1/2}$ . It follows from the Hugoniot relations that the postshock Mach number, and hence  $M_0$  lies in the interval  $[(3/7)^{1/2}, 1]$ . In Fig. 3 is shown the flow profiles for  $\Sigma_0 = 5$  and 15, choosing  $M_0 = 0.7$ .

For typical plasma and pellet parameters of interest,  $\kappa_c \sim 10$  and  $\beta_0/\beta_{\infty} \sim 5$ . Therefore, the ionized ablation channel and cloudlet are weakly diamagnetic objects,  $\beta_0 < 0.1$ , which was to be shown. The parameters  $\Sigma_0$  and  $\beta_0/\beta_{\infty}$  are the two key dimensionless quantities that influence the parallel expansion dynamics treated in Sec. III.

### III. PARALLEL EXPANSION DYNAMICS FOR A DISCRETE CLOUDLET

A fully ionized single-temperature 1D Lagrangian fluid model is well suited to describe the temporal expansion of the cloudlet along the magnetic field lines using the axial profiles in Sec. II as initial conditions. The independent coordinates are  $z_0$  and  $t$ , where  $z_0$  identifies the initial axial position of a Lagrangian fluid element in the range  $0 < z_0 < L_c$ , and  $z(z_0, t)$  denotes its subsequent position at time  $t > 0$ . At the cloudlet-plasma interface, the cloudlet pressure is equal to the plasma pressure at all times. We only follow the early time evolution of the cloudlet up until the pressure in each fluid element has equilibrated with the background plasma pressure. This period is less than the  $\sim 1 \text{ ms}$  time

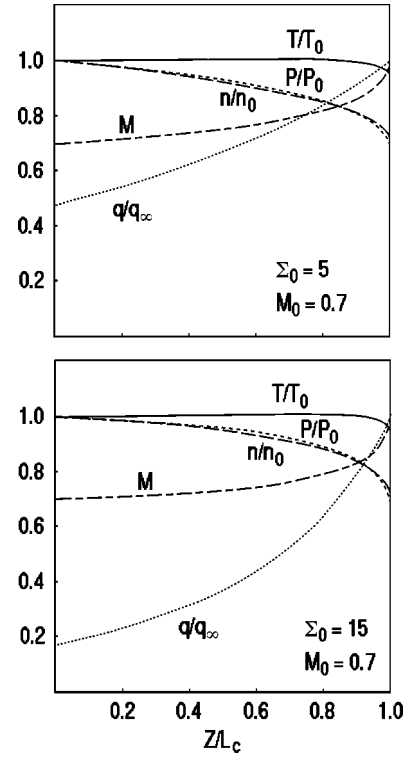


FIG. 3. 1D ablation channel flow profiles.

scale for the homogenization of the density with the background plasma. During this time, the cloud temperature is increasing but still remains well below the background plasma temperature so that the heat flux attenuation model described in Sec. II still holds.

Using rescaled variables:  $x = z_0/L_c$ ,  $\tilde{t} = t/(L_c/\bar{c}_0)$ ,  $\xi = z/L_c$ ,  $\tilde{p} = p/p_0$ ,  $\tilde{n} = n/n_0$ ,  $\tilde{T} = T/T_0$ ,  $\tilde{v} = v_{\parallel}/\bar{c}_0$ , and  $\tilde{c}_0^2 = c_{s0}^2/\gamma$ , the mass, parallel-momentum, and energy conservation equations become

$$\begin{aligned} \tilde{n}(x, \tilde{t}) d\xi &= \tilde{n}(x, 0) dx, \\ \frac{\partial \tilde{v}(x, \tilde{t})}{\partial \tilde{t}} &= \frac{-1}{\tilde{n}(x, 0)} \frac{\partial [\tilde{p}(x, \tilde{t}) + \Pi(x, \tilde{t})]}{\partial x} \\ &= (\gamma - 1) \tilde{n}(x, \tilde{t}) Q(x), \end{aligned} \quad (13)$$

where  $\Pi$  is the von Neuman artificial viscosity introduced to handle shocks. The heat deposition per unit mass consists of the right-going (+) and left-going (−) electron fluxes, and it depends only on the column density, which is constant in time for a given fluid element, namely  $Q(x) = \hat{Q} \Sigma_0 \{G[u^+(x)] + G[u^-(x)]\}$ , where  $G(u) = -K_2(u^{1/2})/2 + u^{1/2}[K_1(u^{1/2}) + K_3(u^{1/2})]/8$ , and

$$u^+(x) = \Sigma_0 \bar{\tau} + \Sigma_0 \int_0^x \tilde{n}(x', 0) dx',$$



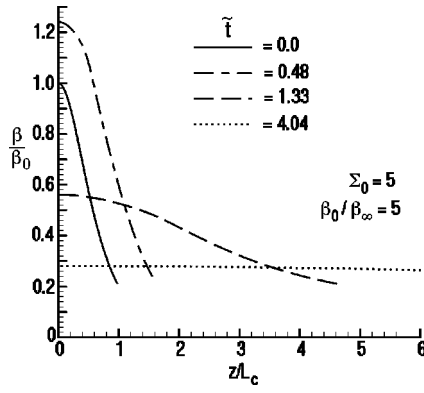


FIG. 4. Axial pressure profile in cloudlet at different sound times  $\tilde{t} = t/(L_c/\bar{c}_0)$ .

$$u^-(x) = \Sigma_0 \int_x^1 \tilde{n}(x', 0) dx', \quad (14)$$

$$\tilde{\tau} = \int_0^1 \tilde{n}(x', 0) dx', \quad \hat{Q} = \frac{q_\infty}{m_i n_0 \bar{c}_0^3}.$$

Thermal heat conduction, radiation loss, and viscous entrainment of the external background plasma along with the flow are not significant processes during the early expansion period. Returning to Eq. (11), we can replace the particle source rate  $G/m_i$  with the particle exit rate  $2\pi r_\perp^2 n_* c_{s*}$  to obtain the value of the “heating quotient”  $\hat{Q}$

$$\hat{Q} = 2\gamma^{3/2} \frac{(1 + \gamma M_0^2)^2}{M_0(1 + \gamma)^2} \left( 1 + \frac{(\varepsilon_{\text{ion}} + \varepsilon_{\text{diss}})\Theta_0}{4\gamma T_0} \right). \quad (15)$$

In view of the mild assumptions about the inlet Mach number  $M_0$ , the numerical value for  $\hat{Q}$  is relatively constant,  $\hat{Q} \approx 5$ . Hence, Eq. (13) depends on only two dimensionless parameters:  $\Sigma_0$  and the pressure (or beta) ratio  $\beta_0/\beta_\infty$  derived in Sec. II. Figure 4 displays the pressure profiles for different times with  $\Sigma_0 = 5$  and  $\beta_0/\beta_\infty = 5$ . Initially, the background pressure counteracts the expansion. This sends a shock wave propagating from the boundary of the cloud into the interior, slightly elevating the midplane pressure above its initial value  $p_0$ . Later the profile relaxes and eventually becomes homogeneous within the cloud at the value of the background pressure. Figure 5 shows the temperature profile for different times using the same parameters as in Fig. 4. Note that at the time  $\tilde{t} = 14.2$  the maximum cloud temperature has reached only  $T \sim 25T_0 = 50 \text{ eV}$ , so it is clear that pressure equilibration with the surrounding plasma takes place well before temperature equilibration. Figure 6 plots the cloudlet half length as a function of time for nominal values of  $\Sigma_0$  and  $\beta_0/\beta_\infty$ .

#### IV. CROSS-FIELD DRIFT DYNAMICS FOR A SINGLE CLOUDLET

The problem is to find the perturbed electrostatic potential in the system consisting of an axially nonuniform cloudlet superimposed on an axially uniform plasma. We use a cylindrical coordinate system attached to the cloudlet at time  $t$ .

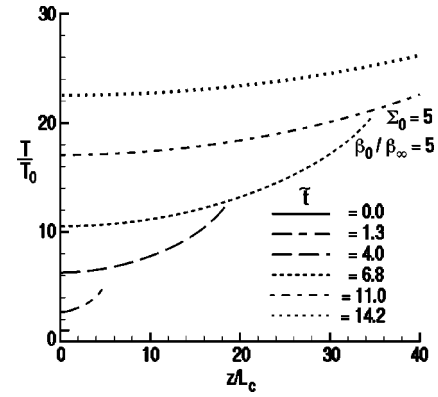


FIG. 5. Axial temperature profiles in cloudlet at different sound times  $\tilde{t} = t/(L_c/\bar{c}_0)$ .

The  $z$  axis is parallel to the applied magnetic field, with  $z = 0$  locating the midplane of the system at that time. The potential  $\varphi(r, \vartheta, t)$  is constant along magnetic field lines. Hence, the transverse cloud motion

$$v_\perp = \frac{\hat{z}}{B} \times \nabla \varphi \quad (16)$$

can be decoupled from the previously treated parallel expansion dynamics. For simplicity, we ignore the rotational transform effect, which is only valid if, during the drift, the length of the cloudlet remains smaller than the connection length  $\sim q\pi R$ .

The transverse one-fluid momentum balance equation is

$$\rho \frac{Dv_\perp}{Dt} = J \times B - \nabla_\perp p + \frac{2p}{R} \hat{x}, \quad (17)$$

where  $D/Dt = \partial/\partial t + v_\perp \cdot \nabla$  is the convective derivative. The last term in Eq. (17) simulates the effect of magnetic curvature, which is often employed when the magnetic field is otherwise treated as being uniform. The unit vector  $\hat{x} = \hat{r} \cos \vartheta - \hat{\vartheta} \sin \vartheta$  points in the direction of the major radius. Taking the cross product of Eq. (17) with  $\hat{z}$  gives the current density

$$\mathbf{J}_\perp = \frac{\hat{z} \times \nabla p}{B} - \frac{2p}{RB} \hat{y} - \frac{\rho}{B^2} \frac{D\nabla_\perp \varphi}{Dt}. \quad (18)$$

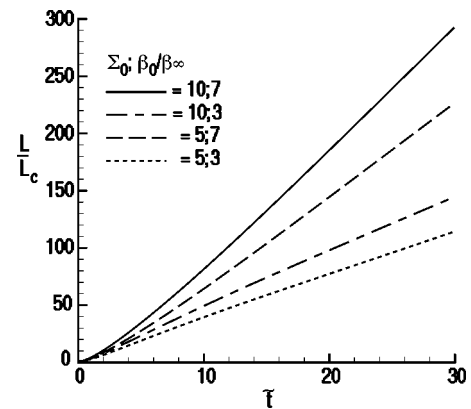


FIG. 6. Cloudlet half length vs time.

The first component is the usual  $\vartheta$ -directed diamagnetic current, which confines the cloud radially, the second term is the vertical curvature and  $\nabla B$  drift current, and the last term is the polarization drift current. The charge continuity equation  $\nabla \cdot \mathbf{J} = 0$  then yields

$$\nabla_{\parallel} \cdot \mathbf{J}_{\parallel} - \frac{2 \sin \vartheta}{BR} \frac{\partial p(r, z, t)}{\partial r} - \frac{\rho}{B^2} \frac{D \nabla_{\perp}^2 \varphi}{Dt} = 0, \quad (19)$$

where in getting the last term we used the identity  $\nabla_{\perp} \cdot D \nabla_{\perp} \varphi / Dt = D \nabla_{\perp}^2 \varphi / Dt$ , recognizing  $\nabla \cdot \mathbf{v}_{\perp} = 0$ .

By symmetry, the parallel current density must be zero at  $z=0$ , so that an integration of Eq. (19) over the half length of the cloud  $0 < z < z_c(t)$  yields

$$J_{\parallel}(z_c) - \frac{2 \sin \vartheta}{BR} \int_0^{z_c} \frac{\partial p(r, z, t)}{\partial r} dz - \frac{\Sigma_{\rho}}{B^2} \frac{D \nabla_{\perp}^2 \varphi}{Dt} = 0, \quad (20)$$

where  $\Sigma_{\rho} = \int \rho dz$  is the half-length column density. The parallel current emitted from the end of the cloudlet  $J_{\parallel}(z_c)$  must match the parallel current carried by an Alfvén wave propagating out into the plasma  $J_{\parallel} = -\mu_0^{-1} \nabla_{\perp}^2 A_{\parallel}$ , where  $A_{\parallel}$  is the wave magnetic vector potential. Since the parallel electric field  $E_{\parallel} = -ik_{\parallel} \varphi + i\omega A_{\parallel} = 0$  in the background plasma, and  $\omega/k_{\parallel}$  is equal to the Alfvén velocity,  $c_{A\infty} = B/(\mu_0 m_i n_{i\infty})^{1/2}$ , Eq. (20) reduces to an equation for the electrostatic potential

$$\frac{\Sigma_{\rho}}{B} \frac{D \nabla_{\perp}^2 \varphi}{Dt} + \frac{B \nabla_{\perp}^2 \varphi}{\mu_0 c_{A\infty}} = - \frac{2 \sin \vartheta}{R} \int_0^{z_c} \frac{\partial p(r, z, t)}{\partial r} dz. \quad (21)$$

It should be noted that the parallel wavelength of the Alfvén wave is  $\sim c_{A\infty} r_{\perp} / v_{\perp}$ , which being on the order of tens of meters greatly exceeds the cloud length by a factor of at least an order of magnitude. Hence, the cloud appears to act like a disk source—its detailed parallel structure has little influence on the outgoing waves.

To simplify the source term in Eq. (21) we next assume a sharp boundary pressure profile:  $\partial p / \partial r = -[p(z, t) - p_{\infty}] \delta(r - r_{\perp})$ . Then both inside and outside the cloud the potential satisfies  $\nabla_{\perp}^2 \varphi = 0$ , with the boundary condition that the electric field vanishes far away from the cloud since we can ignore the finite extent of the plasma ( $r_{\perp} \ll$  plasma minor radius). Because  $\varphi$  is continuous at the boundary  $r = r_{\perp}$ , the solutions in each region are

$$\varphi_{\text{in}} = C(t) r \sin \vartheta, \quad \varphi_{\text{out}} = C(t) r_{\perp}^2 r^{-1} \sin \vartheta. \quad (22)$$

The uniform electric field inside the cloud leads to motion of the cloudlet as a whole in the  $\hat{x}$  direction. The external fringe field allows plasma convection around the cloud as if it were a solid body. To obtain the time dependence  $C(t)$ , we rewrite Eq. (21) in the form of a divergence

$$\nabla_{\perp} \cdot \mathbf{\Gamma} = 2R^{-1} \sin \vartheta \Psi(t) \delta(r - r_{\perp}), \quad (23)$$

where the “flux” is given by

$$\mathbf{\Gamma} = \frac{\Sigma_{\rho}}{B} \frac{D}{Dt} \nabla_{\perp} \varphi + \frac{B}{\mu_0 c_{A\infty}} \nabla_{\perp} \varphi \quad (24)$$

and the cloudlet acceleration function is

$$\begin{aligned} \Psi(t) &= \int_0^{z_c(t)} [p(z, t) - p_{\infty}] dz \\ &= p_0 L_c \int_0^1 \frac{\tilde{n}(x, 0)}{\tilde{n}(x, \tilde{t})} \left[ \tilde{p}(x, \tilde{t}) - \frac{\beta_{\infty}}{\beta_0} \right] dx. \end{aligned} \quad (25)$$

By integrating Eq. (23) over the volume of an infinitesimally thin annular layer, with inner radius  $r = r_{\perp} - \varepsilon$  and outer radius  $r = r_{\perp} + \varepsilon$ , the divergence theorem yields the discontinuity in the flux across the layer

$$(\mathbf{\Gamma}_{r=r_{\perp}+\varepsilon} - \mathbf{\Gamma}_{r=r_{\perp}-\varepsilon}) \cdot \hat{r} = R^{-1} \sin \vartheta \Psi(t). \quad (26)$$

Substituting Eqs. (22) and (24) into Eq. (26) determines the constant  $C(t)$ , and leads us finally to the equation for the velocity of the cloudlet in the major radius direction

$$\Sigma_{\rho} \frac{dv_x}{dt} = - \frac{2B^2 v_x}{\mu_0 c_{A\infty}} + \frac{2}{R} \Psi(t). \quad (27)$$

Here,  $\Sigma_{\rho} = \Sigma_{\rho}^{\text{in}} + \Sigma_{\rho}^{\text{out}} = m_i [n_0 \bar{r} L_c + n_{i\infty} z_c(t)]$ , which remains essentially equal to the constant mass per area of the cloud  $m_i n_0 \bar{r} L_c$  because the initial ion cloudlet density  $n_0$  typically exceeds the plasma ion density  $n_{i\infty}$  by about 4 orders of magnitude. The power carried off by the Alfvén waves, represented by the first term on the right side of Eq. (27), damps transverse motion of the cloud. The rudiments of this picture bear resemblance to magnetohydrodynamics generator, where the electromechanical load taps the kinetic energy of the polarized plasma stream moving across the magnetic field.

The fuel penetration depth can be found *assuming uniform plasma profiles* by a simple integration of Eq. (27) from  $v_x = \pm v_p$  at  $t=0$ , to  $v_x = 0$  at  $t=\infty$ , giving

$$\Delta R = 0.5 \beta_0 \kappa_c r_p \frac{c_{A\infty}}{\bar{c}_0} \langle \tilde{\Psi} \rangle \pm 0.25 \beta_0 \left( \frac{v_p}{\bar{c}_0} \right) L_c \frac{c_{A\infty}}{\bar{c}_0}, \quad (28)$$

where the  $+$ ( $-$ ) sign corresponds to inside (outside) pellet launch, and  $v_p$  is the pellet velocity. Typically  $v_p / \bar{c}_0 \ll 1$  so that the second term on the right side of this expression can be neglected. The toroidal drive integral is defined as

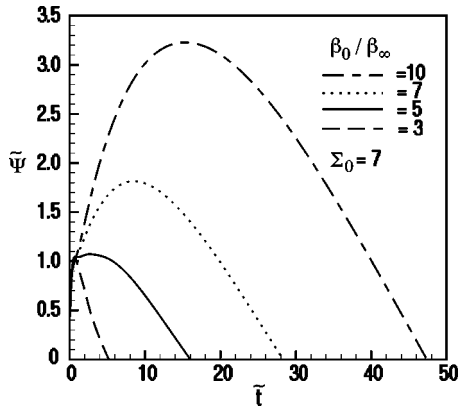
$$\langle \tilde{\Psi} \rangle = \int_0^{\infty} \tilde{\Psi}(\tilde{t}) d\tilde{t}, \quad \tilde{\Psi}(\tilde{t}) = \frac{\Psi}{\rho_0 L_c}. \quad (29)$$

Figure 7 displays the dimensionless acceleration function  $\tilde{\Psi}(\tilde{t})$  vs  $\tilde{t}$ , for different values of  $\beta_0 / \beta_{\infty}$  and  $\Sigma_0 = 7$ . Figure 8 shows the dependence of the toroidal drive integral  $\langle \tilde{\Psi} \rangle$  with  $\beta_0 / \beta_{\infty}$  for some nominal values of  $\Sigma_0$ . For  $\beta_0 / \beta_{\infty} < 10$  it can be approximated by a power law function

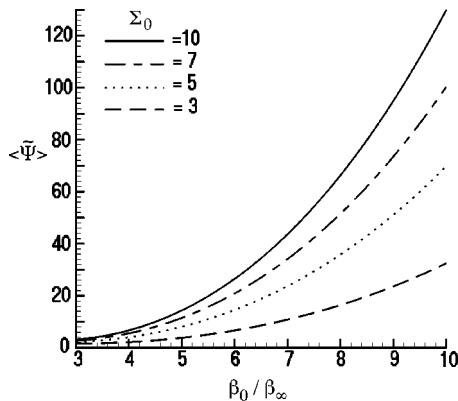
$$\langle \tilde{\Psi} \rangle \cong 0.036 \Sigma_0^{1.1} \left( \frac{\beta_0}{\beta_{\infty}} - 1 \right)^{2.64}. \quad (30)$$

## V. PENETRATION DEPTH SCALING, COMPARISON WITH HFS PELLET INJECTION IN DIII-D, AND PROJECTIONS

In DIII-D pellets were injected from the high-field side of the torus at an angle of  $45^\circ$  above the equatorial plane.

FIG. 7. Cloudlet acceleration  $\tilde{\Psi}(\tilde{t})$  vs  $\tilde{t} = t/(L_c/\bar{c}_0)$ .

The fuel deposition profile was determined experimentally by measuring the change in the density profile  $\Delta n_e$  immediately after injection of the pellet. The density profile change was observed to be much deeper than the calculated and measured penetration depth of the pellet deduced from  $D_\alpha$  line emission recordings. The measured fuel penetration depth  $\Delta R$  can be defined as the distance in major radius between the peak in the  $\Delta n_e$  profile and the peak in the pellet ablation rate, which occurs near the end of the pellet trajectory. Referring to Fig. 4 in Ref. 2 we see that  $\Delta R \approx 20$  cm. To calculate  $\Delta R$  from Eq. (28), we use local pellet and plasma parameters at peak pellet ablation:  $r_p = 0.05$  cm,  $n_{e\infty} = 7 \times 10^{13}$  cm $^{-3}$ ,  $T_{e\infty} = 1.3$  keV,  $B = 3$  T, and  $R = 107$  cm. We find that  $c_{A\infty} = 5.5 \times 10^8$  cm/s,  $\beta_\infty = 0.0081$ , and  $\kappa_c \approx 12.6$ . Then taking  $M_0 = 0.8$  and  $T_0 = 2$  eV, we get  $\beta_0/\beta_\infty = 4.77$ ,  $\Sigma_0 = 5.16$ , and  $\bar{c}_0 = 1.4 \times 10^6$  cm/s, which gives  $\langle \tilde{\Psi} \rangle = 7$ , and finally  $\Delta R = 34$  cm. This result is consistent with the experimental value. The higher calculated value could be expected since we did not take into account plasma profile effects. For this example, Fig. 7 shows that the toroidal acceleration persists for  $\sim 10$  sound times for which the cloud length has increased by 50 times, as indicated by Fig. 6. The cloud length is thus  $2 \times 50 \times L_c = 8.2$  m, which is just slightly less than the connection length  $q\pi R \sim 10$  m. However, it should be noted that when real profile effects are included the cloud length will be substantially reduced as the

FIG. 8. Toroidal drive integral  $\langle \tilde{\Psi} \rangle$  vs  $\beta_0/\beta_\infty$ .

plasma back pressure  $\beta_\infty$  steady increases during the inward drift. The inclusion of real profile effects will also reduce the cloudlet acceleration [Eq. (25)] and  $\Delta R$  from that assuming uniform plasma profiles.

Hence, Eq. (28) should be regarded as an upper limit to the penetration depth for HFS pellet injection. A more convenient  $\Delta R$  scaling formula is given by

$$\Delta R = \frac{0.46 r_p^{1/3}}{M_0 \kappa_c B} \frac{T_{e\infty}^{11/6}}{(\ln \Lambda_{en})^{2/3}} \left( \frac{W}{n_{e\infty}} \right)^{1/6} \langle \tilde{\Psi} \rangle, \quad (31)$$

where  $B$  is in Tesla.

Taking into account Eq. (12), we find that  $\Delta R \sim r_p^{2/3} T_{e\infty}^{5/3} n_{e\infty}^{1/6} B^{-1} \langle \tilde{\Psi} \rangle$ . Since  $\beta_0/\beta_\infty \sim T_{e\infty}$ , and  $\Sigma_0 \sim R^{1/2} n_{e\infty}^{5/6} r_p^{1/3} \ln \Lambda_{ee} T_{e\infty}^{-5/12}$ , the penetration depth increases strongly with values of the plasma temperature, density and pellet radius near the end of the pellet trajectory.

In a large fusion device, with 6 m major radius, the pellet radius near burnout will be  $\sim 0.17$  cm, assuming a pellet velocity of 500 m/s and partial penetration to plasma parameters  $T_{e\infty} \sim 2$  keV,  $n_{e\infty} \sim 10^{14}$  cm $^{-3}$ ,  $R \sim 400$  cm,  $B \sim 5$  T. Our scaling formula gives  $\Delta R = 400$  cm. Of course, this is an overestimate because of the lack of profile effects, as mentioned.

## VI. CONCLUSIONS

An ablation instability (striation oscillations) periodically separates pellet ablation material into discrete field-aligned cloudlets with initially high density and low temperature  $\sim 2$  eV. Although the initial  $\beta$  of the cloudlets is quite small ( $\beta < 0.1$ ), it is typically  $\sim 3$ – $6$  times the local background plasma  $\beta$  along the pellet trajectory. Owing to the  $1/R$  variation of the toroidal magnetic field the excess  $\beta$  generates an uncompensated curvature and  $\nabla B$  drift current inside the cloud. The induced polarization electric field inside the cloud causes rapid cross-field penetration of the cloudlets in the outward major radius direction, thus favoring HFS pellet injection. We formulated the problem by first treating the parallel expansion dynamics to obtain the rate of pressure relaxation in the cloud. This result was then coupled into the model for the electrostatic potential surrounding the moving cloudlet so that we could obtain a simple expression for the  $E \times B$  drift velocity and the penetration depth on the equatorial plane, assuming cloud penetration into a spatially homogeneous plasma.

In view of the favorable scaling of the fuel penetration distance with plasma temperature, density and pellet radius suggested by Eq. (31), the prospect for deep fueling using HFS pellet injection in larger and hotter fusion devices appears promising. However to make realistic predictions future work needs to solve for the drift motion, Eq. (27), with realistic plasma profiles. This entails allowing for nonsteady heat flux and background plasma pressure  $\beta_\infty$  in the parallel expansion dynamics. In addition, it is important to develop 2D and 3D pellet ablation models to refine the estimate of the ablation channel parameters. The helical winding of the magnetic field will become important when the cloud length has become larger than  $q\pi R$ . Not only is the cloud stretched due to magnetic shear when expanding along the magnetic

field, but it also becomes deformed because different segments of the cloud are located at different poloidal angles, and thus drift to different flux surfaces and different flux tubes. In that event the parallel dynamics cannot be decoupled from the cross-field motion. Accordingly, it may be necessary to pursue a 3D cloud drift model, as in Ref. 17.

## ACKNOWLEDGMENTS

This is a report of work supported by the U.S. Department of Energy under Grant No. DE-FG03-95ER54309 and TTUCEP 5-33392. The authors wish to thank M. Fois, B. Kuteev, G. Kocsis, P. Lang, and F. Perkins for valuable interactions.

<sup>1</sup>P. T. Lang, K. Büchl, M. Kaufmann, R. S. Lang, V. Mertens, H. W. Müller, J. Neuhauser, ASDEX Upgrade, and NI Teams, Phys. Rev. Lett. **79**, 1487 (1997).

<sup>2</sup>L. R. Baylor, T. C. Jernigan, S. K. Combs *et al.*, Phys. Plasmas **7**, 1878 (2000).

<sup>3</sup>S. D. Drell, H. M. Foley, and M. A. Ruderman, J. Geophys. Res. **70**, 3131 (1965).

<sup>4</sup>J. E. Borovsky, Phys. Fluids **30**, 2518 (1987).

<sup>5</sup>P. B. Parks, Nucl. Fusion **32**, 2137 (1992).

<sup>6</sup>L. L. Lengyel, IEEE Trans. Plasma Sci. **20**, 663 (1992).

<sup>7</sup>P. B. Parks and R. J. Turnbull, Phys. Fluids **21**, 1735 (1978).

<sup>8</sup>P. B. Parks and M. N. Rosenbluth, Phys. Plasmas **5**, 1380 (1998).

<sup>9</sup>A. K. MacAulay, PhD thesis Princeton University, Princeton, New Jersey, 1993.

<sup>10</sup>S. L. Milora, W. A. Houlberg, L. L. Lengyel, and V. Mertens, Nucl. Fusion **35**, 657 (1995).

<sup>11</sup>J. Balduhn, Plasma Phys. Controlled Fusion **35**, 1413 (1993).

<sup>12</sup>G. Kocsis, J. S. Bakos, R. Burhenn, B. Kardon, S. Kálvin, L. Ledl, G. Mank, G. Petravich, A. Pospieszczyk, and S. Zoletnik, Plasma Phys. Controlled Fusion **41**, 881 (1999).

<sup>13</sup>J. de Kloe, E. Noordermeer, N. J. Lopes Cardozo, and A. A. M. Oomens, Phys. Rev. Lett. **82**, 2685 (1999).

<sup>14</sup>P. B. Parks, Plasma Phys. Controlled Fusion **38**, 571 (1996).

<sup>15</sup>I. Yu. Veselova and V. A. Rozhansky, Sov. J. Plasma Phys. **17**, 817 (1991).

<sup>16</sup>P. B. Parks, J. S. Leffler, and R. K. Fisher, Nucl. Fusion **28**, 477 (1988). [The zero-scattering result follows from Eq. (12) with  $Z_a=0$  and  $p=1$ .]

<sup>17</sup>H. Strauss and W. Park, Phys. Plasmas **5**, 2676 (1998).